



# Characterization of low-pressure high-current cascaded arc plasma in large volumes



S. Avtaeva<sup>a,\*</sup>, V. Gorokhovsky<sup>b,c</sup>, S. Robertson<sup>c</sup>, E. Shun'ko<sup>d</sup>

<sup>a</sup> Institute of Laser Physics SB RAS, Novosibirsk, Russia

<sup>b</sup> Nano-Product Engineering, LLC, Lafayette, CO, USA

<sup>c</sup> University of Colorado, Boulder, CO, USA

<sup>d</sup> AMPRES, Inc., Ypsilanti, MI, USA

## ARTICLE INFO

### Keywords:

Large-volume arc discharge  
Low-pressure  
OES methods  
Langmuir probe  
EEDF  
Retarding potential analyzer  
IEDF  
Modeling  
Drift-diffusion approximation

## ABSTRACT

A comprehensive study of behavior and parameters of the low-pressure (1–20 mTorr) large-area plane-symmetric direct current arc discharge plasma in pure Ar and Ar-N<sub>2</sub> mixtures was carried out. A low-pressure arc discharge was ignited in a large chamber between a planar vacuum arc cathode with magnetic steering of arc spots and a surrounding grounded primary anode while a long-length remote arc discharge was extended toward a remote linear anode parallel to the cathode plate. The arc column moved up and down along the cylindrical cathode target positioned perpendicular to the cathode-to-remote anode direction, following the motion of the cathodic arc spots. Current-voltage characteristics of the low-pressure direct current arc discharge, electron density, electron temperature, electron energy distribution function (EEDF), ion energy distribution function (IEDF) and dissociation of nitrogen molecules in the discharge were studied using electro-technical methods, electrostatic probes, a microwave resonant probe, an ion energy analyzer and optical emission spectroscopy (OES) methods. A number of OES methods were used to determine temperature and density of electrons in the discharge: the  $T_e$  was measured using 1) the  $I_{ArI,415}/I_{ArI,306}$  intensity ratio, 2) an intensity ratio of the (0–0) vibrational bands of 1st negative and 2nd positive systems of N<sub>2</sub>; the  $n_e$  was obtained by 1) the  $I_{ArII,487}/I_{ArI,451}$  intensity ratio and 2) ratio of N<sub>2</sub>(C<sup>3</sup>P<sub>u</sub>,  $v = 1$ ) and N<sub>2</sub>(C<sup>3</sup>P<sub>u</sub>,  $v = 0$ ) populations. In addition, the nitrogen dissociation degree was monitored using  $I_{NII,868.03}/I_{ArI,852.14}$  and  $I_{NII,862.92}/I_{ArI,852.14}$  intensity ratios. Spectral and probe measurements of  $T_e$  and  $n_e$  in the large-area arc discharge show reasonable agreement. The electron population analysis based on the second derivative of the Langmuir probe current-voltage characteristics allowed accurate measurements of electron population parameters in the discharge including EEDF, electron drift velocity along with plasma potential, electron density and energy. Modeling of the low-pressure large-volume arc discharge using the axially symmetric drift-diffusion approximation exhibited good qualitative and acceptable quantitative agreement between calculated plasma parameters and experimental data.

## 1. Introduction

Large area plasmas produced by low-pressure discharges are utilized in industrial-scale plasma processes such as surface treatment, dielectric and semiconductor etching and thin film deposition [1,2]. Large area plane-symmetric low-pressure direct-current (DC) glow discharge in Ar and in Ar-N<sub>2</sub> mixtures was studied in our previous work [3]. The combination of different plasma diagnostic techniques including electrostatic probes, MW resonance “hairpin” probe and optical spectroscopy were applied to obtain reliable information regarding physical processes in the discharge. The electron density in the glow discharge was found varies from  $1 \cdot 10^7$  cm<sup>-3</sup> to  $4 \cdot 10^{10}$  cm<sup>-3</sup> and the electron

energy distribution function (EEDF) has two populations of electrons: the main non-Maxwellian population with a mean electron energy of  $\approx 0.3\text{--}0.4$  eV and a second, small Maxwellian population of “hot” electrons, with a mean electron energy  $\approx 1.0\text{--}2.5$  eV [3].

More powerful source of dense plasma, which can be used in various technologies such as surface engineering processes [4], electric propulsion [5], and isotope separation [6] is a low-pressure arc. The low-pressure (LP) arc as well as the vacuum arc was studied intensively from 1950s [7–10]. Properties of *large area* LP arc discharges are different from properties of the conventional vacuum arc discharges and are less investigated and understood. The arc discharge plasma generated in the large volumes by using stationary thermion emission cathodes was

\* Corresponding author.

E-mail address: [s\\_avtaeva@mail.ru](mailto:s_avtaeva@mail.ru) (S. Avtaeva).

previously investigated by Gekelman et al. [11], Leneman et al. [12], Awasthi et al. [13], Hong et al. [14]. In the named works, the low-pressure arc discharge plasma had a stationary distribution of plasma parameters across the vacuum chamber.

In the present paper, the parameters of the low pressure arc discharge operating in a large vacuum chamber with atmospheres of Ar or Ar-N<sub>2</sub> mixtures at the pressures ranging from 1·10<sup>-3</sup> to 2·10<sup>-2</sup> Torr are obtained by the combination of the Langmuir probes, hairpin probes and OES plasma diagnostics techniques. The large area cascaded arc discharge at such a low pressure has not been previously studied in a comprehensive collection of the diagnostic techniques. The primary goal of this paper is characterization of a composition of the large area arc plasma commonly used in industrial plasma vapor deposition and chemical vapor deposition coatings, plasma cleaning, ionitriding and other surface treatment processes with the emphasis on plasma diagnostics methodology and its experimental verification.

This paper presents the comparison of the measured and modeled parameters of the large-area plane-symmetric DC arc discharges in Ar and Ar-N<sub>2</sub> mixtures. The arc discharge is generated by the cathodic arc spots of the vacuum arc cathode, which are moving at high speeds across the plasma volume. More than one anode is used to support cascaded arc discharge in long vacuum chamber. The optical emission spectroscopy (OES) methodologies previously developed for studying the large area low-pressure glow discharge in [3] were applied in this study in combination with other diagnostic techniques such as different probes and retarding potential analyzer. The electron temperature  $T_e$  was obtained using 1) an intensity ratio of two ArI lines, 2) an intensity ratio of the (0–0) vibrational bands of 1st negative and 2nd positive systems of nitrogen. The electron density  $n_e$  was obtained by 1) an intensity ratio  $I_{\text{ArII}, 487}/I_{\text{ArI}, 451}$  of ArII and ArI lines and 2) ratio of N<sub>2</sub>(C<sup>3</sup>Π<sub>u</sub>,  $v = 1$ ) and N<sub>2</sub>(C<sup>3</sup>Π<sub>u</sub>,  $v = 0$ ) populations. In addition, the nitrogen dissociation degree was monitored using  $I_{\text{NI}, 868.03}/I_{\text{ArI}, 852.14}$  and  $I_{\text{NI}, 862.92}/I_{\text{ArI}, 852.14}$  intensity ratios. Spectral and probe measurements of  $T_e$  and  $n_e$  obtained in the large-area arc discharge have demonstrated reasonable agreement. The electron population analysis based on the second derivative of the Langmuir probe current-voltage ( $I$ -V) characteristics allowed accurate measurements of electron population parameters in the discharge including EEDF, electron drift velocity, plasma potential, electron density and energy.

The structure of the paper is following; section 2 briefly describes experimental setup and diagnostic methods, section 3 presents the large-area arc discharge parameters measured by probes and OES and section 4 contains low-pressure arc modeling. Finally, Application A is dedicated to analysis of the electron population based on the second derivative of the Langmuir probe  $I$ -V characteristics.

## 2. Experimental setup and diagnostic methods

To develop the cascaded large area LP arc discharge we use a remote anode together with a primary anode [15]. The remote anode draws out electrons from the primary discharge and forces them to move for a long distance producing large-area plasma. The experimental setup is shown in Fig. 1. The discharge was ignited in the horizontal rectangular discharge chamber of  $2 \times 1 \times 0.25 \text{ m}^3$ . The primary arc (PA) discharge was ignited between a planar stainless-steel cathode separated from the discharge chamber by a chevron baffle which served together with the chamber walls as a primary anode. The cathodic vacuum arc spots moved up and down along the periphery of the vertical cathode under the influence of a magnetic steering system which utilized a set of permanent magnets positioned behind a 1-m long cathode.

The remote arc (RA) discharge, powered by a RA power supply utilizing two Miller XMT 456 welding power supplies connected in series with 180 V open circuit voltage, extended horizontally beyond the chevron baffle, along the discharge chamber between the cathode and the main remote anode, forming a  $\approx 1.5 \text{ m}$  long RA column. The resistances both in the primary arc circuit R1 and in the remote arc

circuit R2 were approximately 0.5 Ohm each. An additional intermediate remote anode was installed at about mid-point location between the cathode and the main remote anode. The intermediate anode was connected to the positive terminal of the RA discharge power supply via a variable resistor R3.

All experiments were performed with a primary arc current of 75 A while the anode currents for both intermediate or mid anode and main remote anode were varied from 5 to 200 A. Gas pressure was varied from 2·10<sup>-3</sup> to 25·10<sup>-3</sup> Torr and the Ar-N<sub>2</sub> mixture composition was changed from pure argon to pure nitrogen. A set of multi-channel ion-collection probes was placed equidistantly along the vertical axes perpendicular to the cathode-anode horizontal axes within the distance equal to the length of the cylindrical cathode target to determine the vertical movement dynamics of the RA plasma column as shown in Fig. 1b. Each of the ion collecting probes comprised a stainless steel (SS) disk, 5 mm in diameter positioned perpendicular to the remote arc column axes and biased negatively to  $-20 \text{ V}$  below the floating shield which surrounded the probes. The Langmuir and hairpin probes were placed at the discharge axis as is shown in Fig. 1. The signals of these probes can be collected simultaneously providing information of ion current density distribution in the direction perpendicular to the cathode-remote anode axis.

The cylindrical Langmuir probe ESPION was manufactured by Hiden Analytics. The Langmuir probe had a 150  $\mu\text{m}$  diameter tungsten wire filament with an active length of 10 mm, which was enclosed in an alumina tube. The scanning speed of the probe's  $I$ -V measurements were typically set to 1 V/0.66 s. The details on the  $T_e$  and  $n_e$  measurements using the Langmuir probe technique in the arc discharge plasma are described elsewhere [3]. The Hiden Analytics hairpin resonator was fork-shaped and has 75 mm length and 20 mm gap. The principle of measuring electron density by the hairpin probe is based on the relative shift of its resonance frequency in plasma from the resonance frequency in vacuum [16]. The ion energy distributions functions (IEDFs) in the RA discharge column were measured by the scanning gridded retarding potential analyzer (RPA) probe shown in Fig. 1b, which was immersed within the RA discharge plasma. The RPA could be moved laterally and rotated around its vertical axes perpendicular to the cathode-remote anode lateral axes all owing its front orifice to either face the cathode or the remote anode. Five grids and anion collector are employed in the RPA. The ion energy distribution function  $f(V)$  was extracted by differentiation of the collector ion current  $I_c(V_a)$  with respect to the voltage applied to the analyzing grid  $V_a$  [18].

In addition, the electron temperature  $T_e$  and density  $n_e$  were measured using optical emission spectroscopy (OES) technique. In the Ar discharge  $T_e$  was measured by the intensity ratio of two ArI lines 415.86 and 306.65 nm  $I_{\text{ArI}, 415}/I_{\text{ArI}, 306}$ , which is a function of the  $T_e$  under conditions of coronal equilibrium [16]. In the Ar-N<sub>2</sub> discharge  $T_e$  was also estimated using the intensity ratio of the (0–0) vibrational band of the N<sub>2</sub> 1st negative system (391.4 nm) and the (0–0) vibrational band of the N<sub>2</sub> 2nd positive system (337.1 nm) [3]. The electron density  $n_e$  in the argon RA discharge was obtained using the intensity ratio  $I_{\text{ArII}, 487}/I_{\text{ArI}, 451}$  of ArII 487.98 nm and ArI 451.07 nm lines [3]. In the Ar-N<sub>2</sub> RA discharge we also estimated  $n_e$  using the contour graph of N<sub>2</sub>(C<sup>3</sup>Π<sub>u</sub>,  $v = 1$ ) / N<sub>2</sub>(C<sup>3</sup>Π<sub>u</sub>,  $v = 0$ ) population ratios [19]. The nitrogen dissociation degree was monitored using  $I_{\text{NI}, 868.03}/I_{\text{ArI}, 852.14}$  and  $I_{\text{NI}, 862.92}/I_{\text{ArI}, 852.14}$  intensity ratios [10]. Four HR-4000 Ocean Optics spectrometers with full bandwidth of 199–972 nm and having optical resolutions of  $\approx 0.03 \text{ nm}$  (1200 lines/mm gratings) and high sensitivity detectors were utilized to measure intensities of the spectral lines. Light was gathered from a volume having a length of  $\approx 1.5 \text{ m}$ . A collimated 30 cm long focus lens collected light along very narrow volume near the center of the chamber and focused it into a fiber optic cable divided in 4 channels and connected to the entrance slits of the spectrometers. The relative sensitivity of the devices with wavelength was calibrated using Ocean Optics Deuterium Tungsten-Halogen Calibration Light Source DH-2000-CAL.

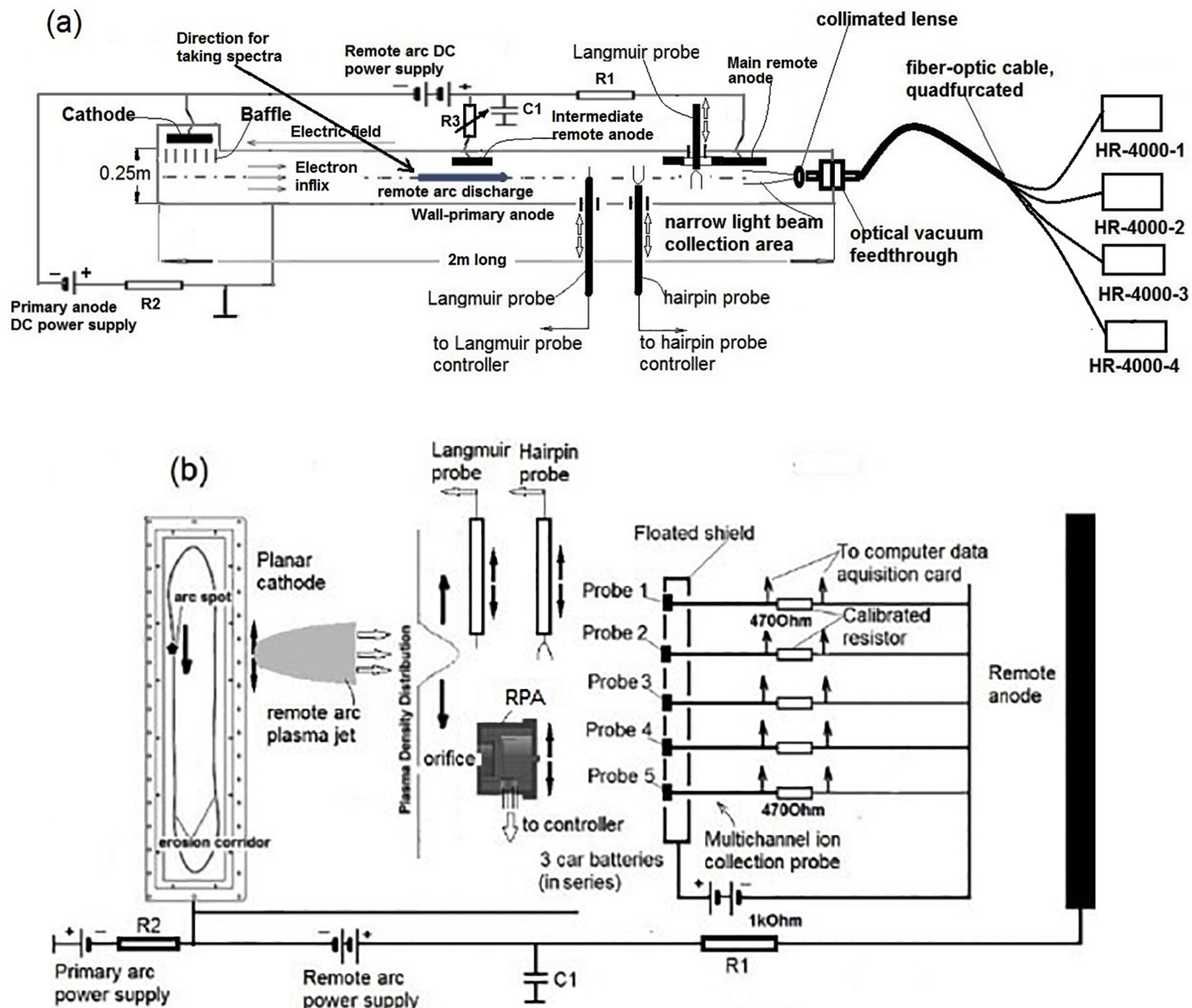


Fig. 1. The low-pressure remote arc discharge setup in long chamber: (a) planar view; (b) side view.

### 3. Experimental results and discussion

The RA discharge appeared to be spatially uniform in the lateral direction while in a direction perpendicular to the cathode-remote anode axis the RA column was observed, which was moving up and down dragged by the motion of the cathodic arc spots. The  $I$ - $V$  characteristic of the remote arc discharge in argon is shown in Fig. 2a. The  $V$ - $P$  characteristics of remote and intermediate anodes are shown in Fig. 2b and c. The remote anode voltage  $U_{RA}$  rose with increasing remote anode current  $I_{RA}$  from 20 A to  $\approx 60$  A and saturated at  $I_{RA} > 60$  A.  $U_{RA}$  was decreased when the discharge pressure was increased. This effect can be also seen from  $V$ - $P$  characteristics of the intermediate anode in different gas mixtures, Fig. 2c, which also shows that adding nitrogen to argon increased the remote anode voltage drop.

A typical set of signals from the four disk ion collector probes located at different heights from the bottom of the chamber is shown in Fig. 3. It is demonstrating spikes of the ion currents collected by each disk-probe when the remote arc column is crossing the probe during its vertical movement, driven by the vertical motion of the cathodic arc spots along the cathode evaporation surface in the vertical direction perpendicular to the cathode-remote anode axes.

The velocity of the arc plasma column movement was further verified by the measurements taken by RPA and OES. For this purpose the estimated frequencies of the picks of the ion collecting signals collected by the RPA or OES, the signals taken at the selected spectral lines were compared with the frequencies  $f_{c.s.}$  of the picks of the ion current density signals collected by the multi-channel probe. Assuming, that cathodic arc spot is traveling up and down along the cathode target of the length  $L_{target}$ , the characteristic velocity of the cathodic arc spots can be estimated as  $V_{c.s.}$  (m/s)  $\approx L_{target}$  (m)  $f_{c.s.}$  (1/s). The frequencies estimated from RPA and OES measurements ranges from 10 to 100 Hz in a good agreement with the frequencies estimated from the multi-channel probe measurement resulting in cathodic arc spot velocities ranging from 1 to 10 m/s.

It should be noted, that usually there are more than one traveling arc spot on the SS cathode at currents exceeding 50 A, which is the minimum arc current for one spot on SS. This can explain that some of the disk-probes can show the signal outside of the time-shift line. It was found that the arc spot speed increased with the remote arc current in agreement with the vacuum arc retrograde movement law [10]. One can see that each signal representing an arc column crossing the probe is split in a number of the higher frequency fringes. This can be

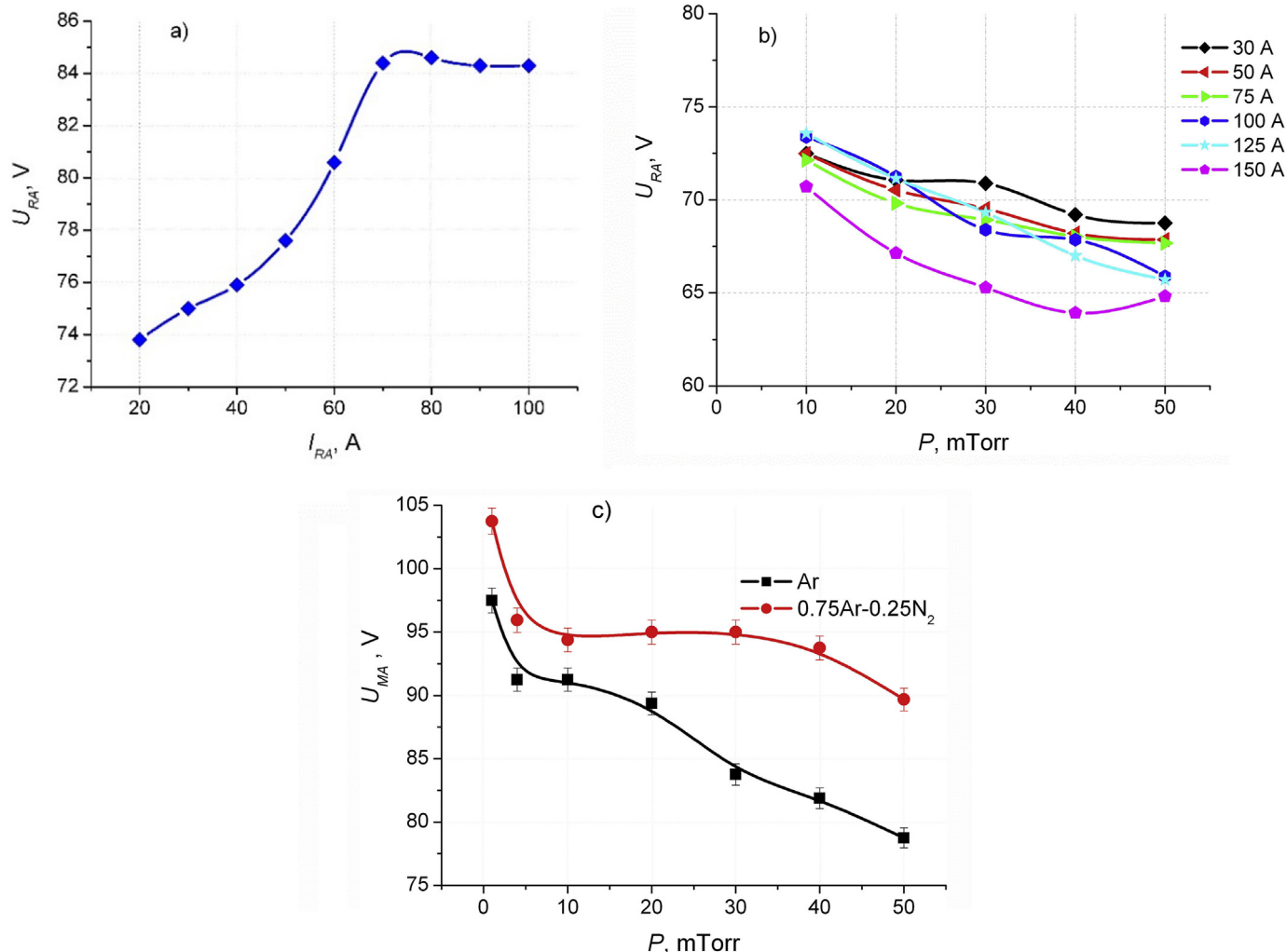


**Fig. 2.** (a) The  $I$ - $V$  characteristics of RA discharge in argon at  $2.5 \cdot 10^{-3}$  Torr, (b) the remote anode voltage in Ar versus pressure at different remote arc currents, and (c) intermediate anode voltage versus pressure at remote arc current 20A. The estimated error in these measurements does not exceed 10%.

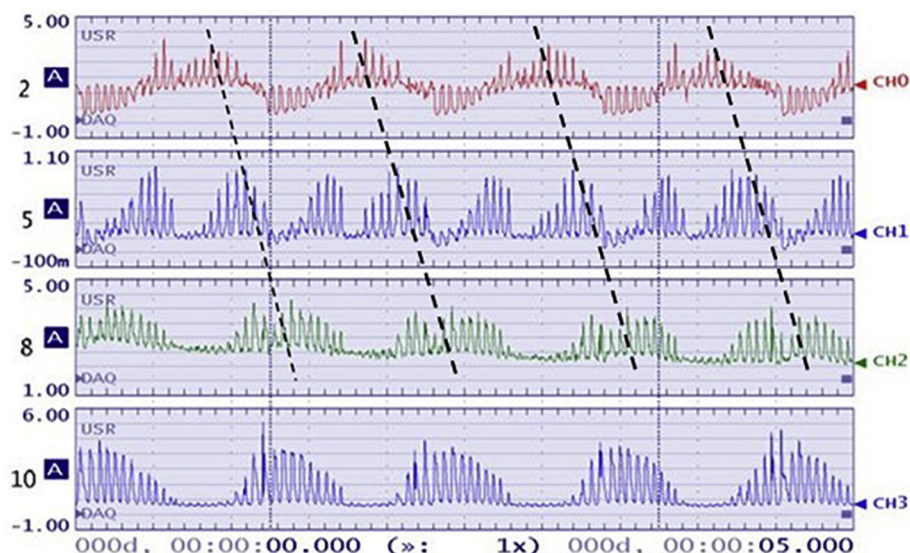


**Fig. 3.** Multi-probe ion current signals collected simultaneously from 4 disk-probes, located at different vertical positions parallel to the cylindrical cathode target axis with -20 V applied to active probes relative to the surrounding metal shields. The primary arc current  $I_{PA}$  was 150A and the remote anode current  $I_{RA}$  was 100A. Probe 2 was located at high 0.3 m and probe 5 was located at 0.1 m above the cathode target centerline, probe 8 and 10 were located at high -0.1 m and -0.2 m below the cathode target centerline. One small division on the abscissa scale equals to 0.1 s. The dashed lines indicate the shift in a time between the collecting signals of the disk-probes located at different heights.

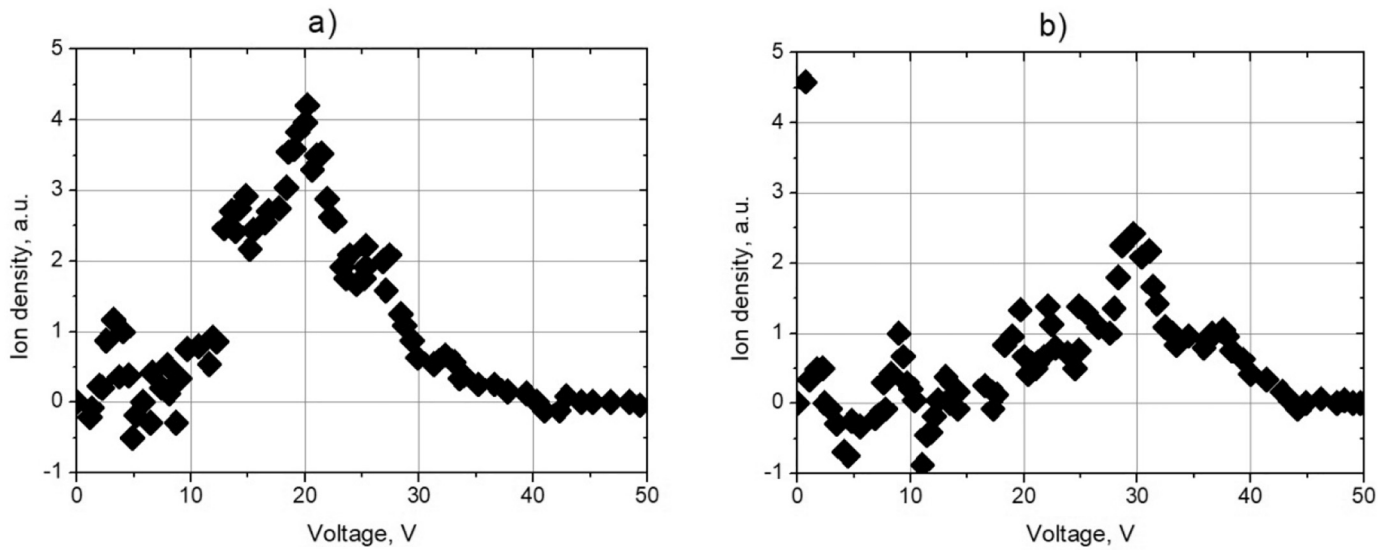


**Fig. 4.** The IEDFs of the RA plasma in argon at  $P = 2 \cdot 10^{-3}$  Torr: (a)  $I_{RA} = 300\text{A}$ , RPA facing cathode; (b)  $I_{RA} = 300\text{A}$ , RPA facing anode.

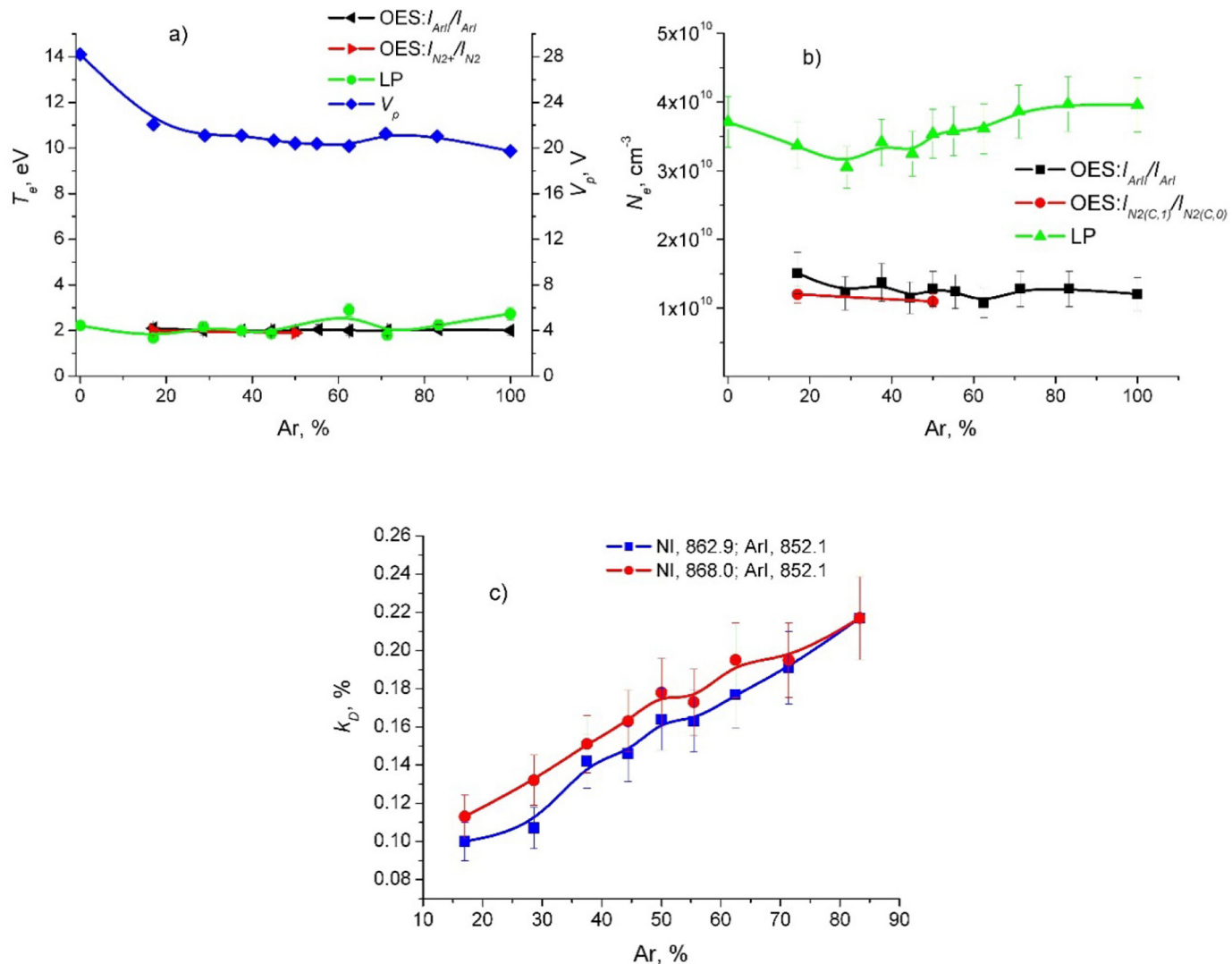


**Fig. 5.** (a)  $T_e$ ,  $V_p$  and (b)  $n_e$  obtained with the OES and with the Langmuir probe, as well as (c) the N<sub>2</sub> dissociation degree in the arc discharge as functions of the Ar fraction in Ar-N<sub>2</sub> mixtures; with  $P = 2 \cdot 10^{-3}$  Torr,  $I_{PA} = I_{RA} = 75\text{A}$ . The estimated error in these measurements does not exceed 10%.

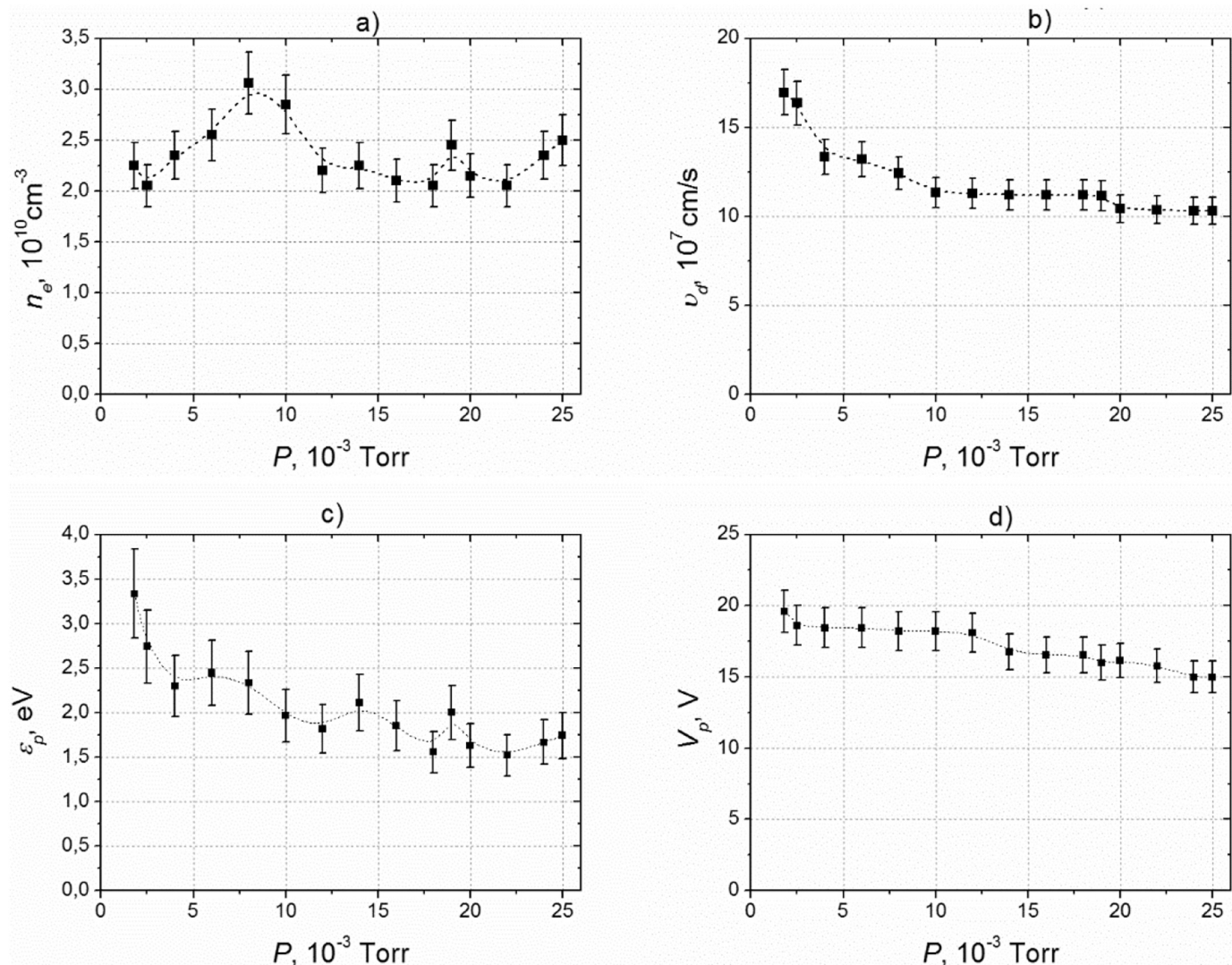


**Fig. 6.** The electron density  $n_e$ , electron drift velocity  $v_d$ , electron energy  $\epsilon_p$  (corresponding to the most probable electron velocity  $v_p$  for Maxwellian electrons moving in the reference system with the drift velocity  $v_d$ ), and the plasma potential  $V_p$  versus Ar-gas pressure  $P$  at the distance from the anode  $d_a > 10 \text{ cm}$  and at  $I_{RA} = 75 \text{ A}$ . The calculated standard deviation does not exceed 15–20% for  $\epsilon_p$  and 10% for  $V_p$ .

attributed to the helical movement of the cathodic arc spots steered by the external longitudinal magnetic field, which rotates the cathodic arc spots around the cathode target cylinder and periodically moves the cathodic arc spots to the side of the cathode target cylinder opposite to the side facing the remote anode. This motion results in the periodically increase of the remote arc plasma impedance and decrease of the plasma density in the remote arc discharge column with the annular frequency corresponding to the annular frequency of rotation of the cathodic arc spots. The estimated speed of the vertical movement of the arc spots ranged from 1 to 10 m/s which is typical for an arc current of  $\approx 100\text{A}$  [10].

The ion energy distribution functions obtained with the RPA in argon RA plasma are shown in Fig. 4. It can be seen that in the RA plasma with  $I_{RA} = 300\text{A}$  there were well-defined groups of energetic ions, having the mean energy of  $\approx 20\text{--}30 \text{ eV}$  both when the RPA faced the cathode (a) and the anode (b) with full width at half maximum (FWHM) of  $\approx 10\text{--}15 \text{ eV}$ . The higher ion energies taken from the anode side than from the cathode side can be explained by acceleration of the ions in the electric field of the arc column.

The plasma potential determined from the potential at which the Langmuir probe  $I\text{-}V$  curve had its maximum derivative was 16–20 V, and its value was depended weakly on the RA current. The  $T_e$  was

decreased slightly with RA current  $I_{RA}$  and with the gas pressure  $P$  increase and was in the range of 1.8–3.0 eV. The character of the  $T_e$  dependencies on  $I_{RA}$  and  $P$  measured by the Langmuir probe are like that obtained using the intensity ratios, but  $T_e$  values measured by the probe were higher by  $\approx 0.5 \text{ eV}$  than that obtained by the intensity ratios.

The electron density in the low-pressure arc was increased with the both  $I_{RA}$  and with gas pressure  $P$ . In Ar-N<sub>2</sub> arc discharges, both  $I_{\text{ArII},487}/I_{\text{ArI},451}$  and  $n_{N_2}/c_1/n_{N_2}$ ,  $c_1/n_{N_2}$ ,  $c_0$  ratios show close values of  $n_e$  at  $P = 2.5 \cdot 10^{-3} \text{ Torr}$ . The  $n_e$  was increased from  $2.5 \times 10^9$  up to the  $2.5 \times 10^{10} \text{ cm}^{-3}$  when the remote anode current was increased from 5 up to the 75 A. Under most discharge conditions, the Langmuir probe indicated a  $n_e$  of about 2–3 times higher than what the OES gave while the microwave hairpin probe indicated a  $n_e$  similar to the OES. The difference appears due to the Langmuir probe measurements being local, while the OES measurements are non-local, averaged over whole discharge length. The ionization degree in the RA discharges was in the range of  $\approx 2.5 \times 10^{-5} - 2.5 \times 10^{-4}$ .

In Fig. 5 the plasma potential, electron temperature and density as well as the N<sub>2</sub> dissociation degree as a function of the argon fraction in Ar-N<sub>2</sub> mixtures are shown. The electron density is found to be 1–2 orders of magnitude greater than that measured at the low pressure glow discharge in the similar pressure range [3] and comparable to the

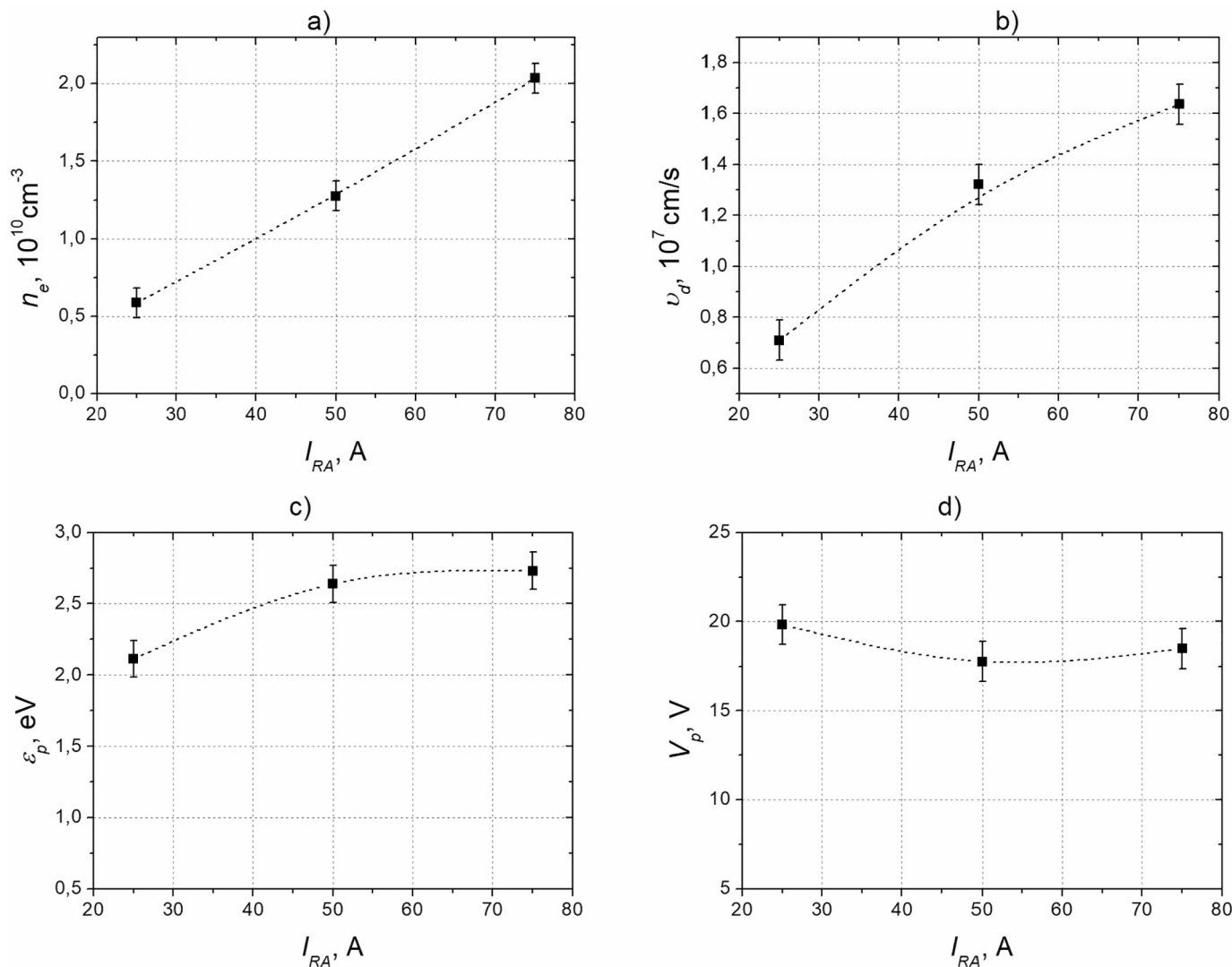
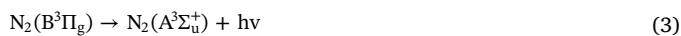


**Fig. 7.** The electron density  $n_e$ , electron drift velocity  $v_d$ , electron energy  $\epsilon_p$ , corresponding to the most probable electron velocity  $v_p$  (for the Maxwellian electrons moving in the reference system with the drift velocity  $v_d$ ), and plasma potential  $V_p$ , versus the remote anode current  $I_{RA}$  at the distance from the anode  $d_a > 10 \text{ cm}$  and at argon pressure  $p_{Ar} = P = 2.5 \cdot 10^{-3} \text{ Torr}$ . The calculated standard deviation does not exceed 15% for  $n_e$ , 20% for  $v_d$  and 10% for  $\epsilon_p$ ,  $V_p$ .

values obtained in a stationary thermionic arc plasma [12–14].

The values of  $V_p$ ,  $T_e$  and  $n_e$  were weakly depended on the mixture composition at Ar fractions  $> 20\%$  because ionization potentials of the Ar atoms (15.76 eV) and N<sub>2</sub> molecules (15.6 eV) are close. The N<sub>2</sub> dissociation degree increased with the Ar fraction. The dependence is opposite to the case of the large-area low-pressure glow discharge [3] in which N<sub>2</sub> dissociation degree decreased with Ar fraction. The difference is because of 2–3 eV higher  $T_e$  in the low-pressure arc as compared with the low-pressure glow discharge. Estimations provided were showed, that  $T_e$  and  $n_e$  changed a little with Ar fraction, the Ar<sub>m</sub><sup>\*</sup> density rises with increasing Ar fraction, and the most probable mechanism of N<sub>2</sub> dissociation under low-pressure arc conditions is excitation transfer from Ar<sub>m</sub><sup>\*</sup> to N<sub>2</sub>:



The detailed analysis of the electron population in the remote arc discharge followed the methodology described by Shun'ko [20] and

previously applied to the glow discharges [3] is presented in the Appendix (Supplementary data). The electron population in the vicinity of the remote anode, at the distances  $d_a$  from the anode ranging from 0 to 5 mm, was studied using the Langmuir probe in the electron-collecting mode at an electron-repelling potential  $V_f < V < 0$ , where  $V_f$  is the floating potential.

The parameters of the electron population in the area near the remote anode (see the Appendix) were compared to the parameters of the electron population within the bulk remote arc plasma far from the chamber walls and remote anode. The results of this analysis have demonstrated a considerable difference of plasma properties in the area near the remote anode vs. bulk plasma within the remote arc plasma column.

Parameters of the electron population far from the chamber walls and electrodes ( $d_a > 10 \text{ cm}$ ) were measured as functions of the Ar pressure and the remote anode current. In the Fig. 6 the plasma potential  $V_p$  and parameters of the electron population ( $n_e$ ,  $v_d$  and  $\epsilon_p$ ) are shown as the functions of the argon pressure  $P$  in the range of  $(2-25) \cdot 10^{-3} \text{ Torr}$ . The error bars shown in the Figs. 6, 7 are the standard deviations calculated at 95% confidence level over 10 values of the experimental data.

The measured electron energy  $\epsilon_p$  corresponds to the most probable

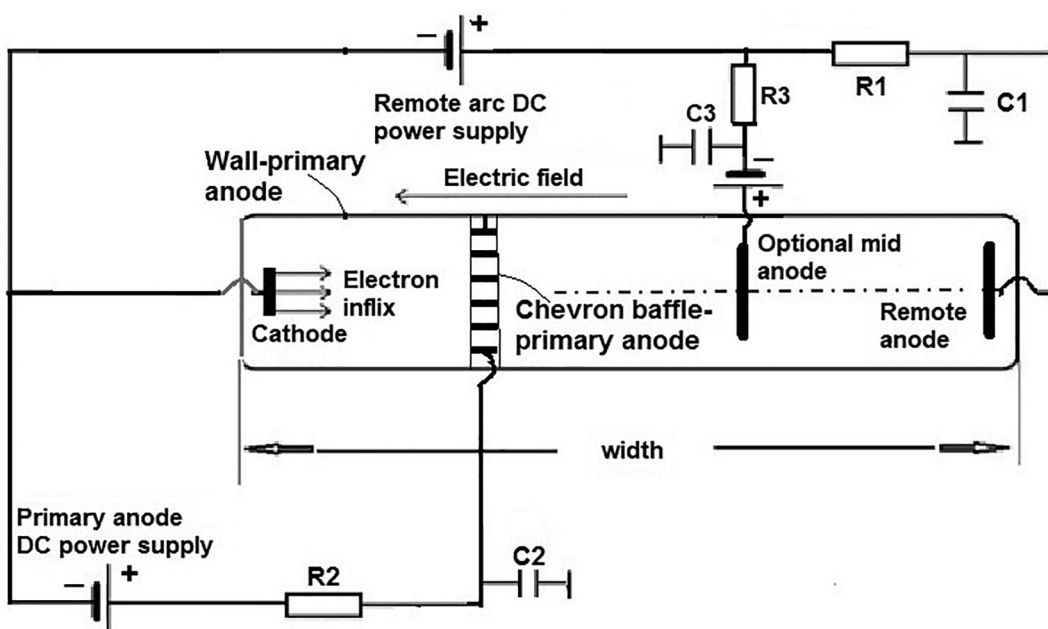


Fig. 8. Scheme of the remote arc discharge model setup.

Table 1

The reactions included in the model. The cross-sections for the electron impact reactions were taken from the Phelps database [24].

No.	Type	Formula	Energy (eV)
R1	Elastic	$e + Ar \rightarrow e + Ar$	0
R2	Excitation	$e + Ar \rightarrow e + Ar^*$	11.5
R3	Superelastic	$e + Ar^* \rightarrow e + Ar$	-11.5
R4	Ionization	$e + Ar \rightarrow e + Ar^+$	15.8
R5	Ionization	$e + Ar^* \rightarrow e + Ar^+$	4.24
R6	Penning ionization	$Ar^* + Ar^* \rightarrow e + Ar^+ + Ar$	-
R7	metastable quenching	$Ar^* + Ar \rightarrow 2Ar$	-

thermal velocity  $v_p = \sqrt{2\varepsilon_p/m}$  of the Maxwellian electrons in the system moving with the drift velocity  $v_d$  found from the measurements. The plasma potential and the electron density have values close to those obtained by the traditional Langmuir probe calculations without data corrections, and the electron energy corresponding to the most probable electron velocity  $v_p$  for Maxwellian electrons moving in the reference system with drift velocity  $v_d$  was close to the average electron energy corresponding to the electron temperature  $T_e$  obtained by the traditional Langmuir probe data treatment technique without corrections.

Fig. 7 shows plasma potential  $V_p$  and parameters of the electron population ( $n_e$ ,  $v_d$  and  $\varepsilon_p$ ) versus the remote anode current  $I_{RA} = I_a$  at  $P = 2.5 \cdot 10^{-3}$  Torr. As it can be seen from the Fig. 7, the electron density  $n_e$  and the drift velocity  $v_d$  are increased strongly with the  $I_{RA}$  growth, while the plasma potential,  $V_p$ , and the electron energy,  $\varepsilon_p$ , are changed slightly. All the electron parameters plotted in the Figs. 6, 7 were calculated with the corrections described in the Appendix.

The values of the electron drift velocities presented in Fig. 7 enabled one to find the corresponding parameters  $E/N_g$  (see Table 6.4, Drift Velocity in Argon at 293 K, in [21]). The density of the neutral argon-gas atoms can be found from the equation  $N_g = (T_0/T_g)N_0$ , where  $N_0$  and  $T_0$  are Ar density and temperature near the probe position and  $T_g$  is the gas temperature in the chamber. At the pressure of  $2 \cdot 10^{-3}$  Torr, measured at 293 K, the gas density in the chamber, at 473 K, is  $N_g = 4.08 \times 10^{19} \text{ m}^{-3}$ , and the average value of the electrical field  $E$  expected for the drift velocities  $v_d \approx 10^4 \text{ m/s}$  shown in Figs. 6, 7 is  $E < 0.1 \text{ V/cm}$  with acceptable precision from the data presented in Figs. 6, 7 by taking into account the distribution of the plasma potential

measured. It can be seen that electric field within arc column is more than 3 times lower than that in the area near the remote anode (for details see the Appendix).

#### 4. Low-pressure arc modeling

The electric setup of the axisymmetric cascaded arc model considered in this work, mimicking the experimental setup shown in Fig. 1, is shown schematically in Fig. 8. The cathode and remote anode were positioned at opposite ends of a cylindrical metallic discharge tube. The cathode was separated from the rest of the discharge volume by a chevron baffle. The baffle was electrically connected to the discharge tube, which together formed the combined primary anode for the primary arc discharge conducted between the cathode and the discharge tube walls with or without chevron baffle. An optional mid-anode was positioned in the middle between the cathode and a remote anode. Each anode is provided with an independent electric circuit including power supply, ballast resistor and blocking capacitor.

The low-pressure large-volume arc studied experimentally was modeled using an axially-symmetric drift-diffusion approximation with commercial COMSOL FEM software [20]. The arc discharge was ignited between a small cathode mimicking the vacuum arc cathode spot and the primary arc anode consisting of the discharge tube walls and the chevron baffle. The primary arc feeds a large area remote arc discharge in the space between the chevron baffle and the remote arc anode. The cathode and remote anode are metal discs with small, 2 mm, thickness ranging from 2 to 6 mm. To mimic the cathode spot emission, the diameter of the cathode was chosen as 1 cm, while the diameter of the remote anode was 20 cm. The thermionic electron current density emitted by the cathode (the electron influx current) and the argon pressure were the input parameter of the model.

The drift-diffusion model was used to model the low-pressure arc discharge in argon. The core of the numerical model is the transport equations, which can be expressed in the same form for all species [22,23]:

$$\frac{\partial n_\alpha}{\partial t} + \nabla \cdot \Gamma_\alpha = R_\alpha \quad (5)$$

where the subscript  $\alpha$  denotes either electrons (e), ions (i) or various neutral particles (n), both excited and in the ground state;  $n_\alpha$  is the

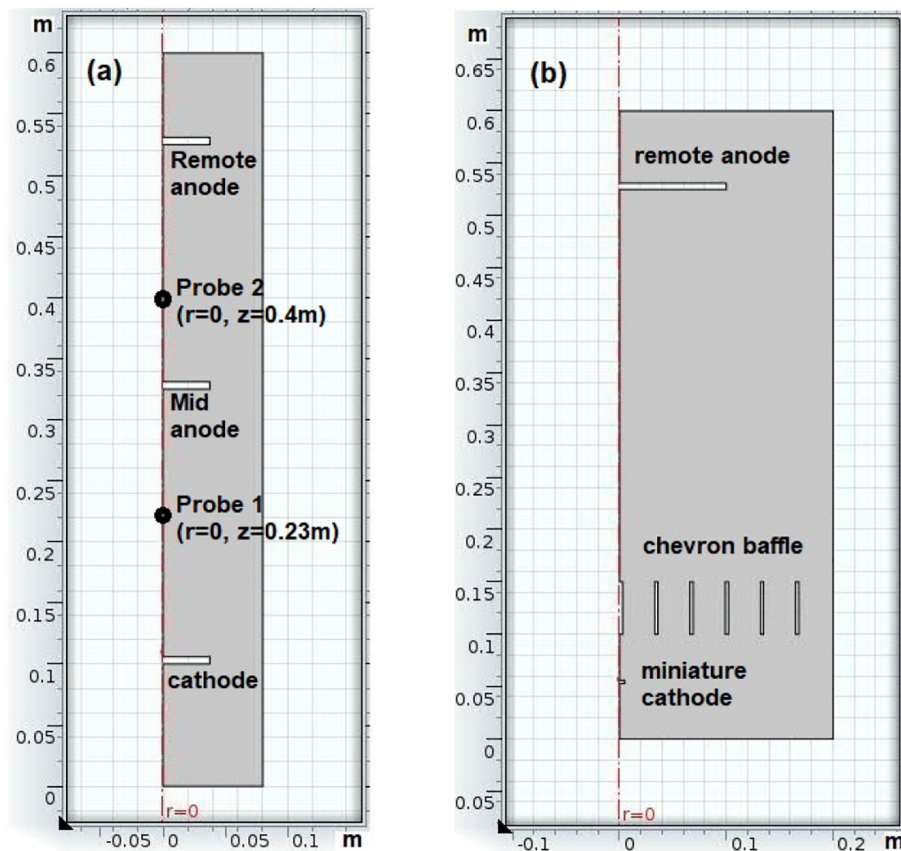


**Fig. 9.** Model geometry (a) with three anodes and (b) with baffled miniature cathode and remote anode.

number density of the corresponding species;  $\Gamma_a$  is its flux and  $R_a$  is a source term.

The excited particle fluxes  $\Gamma_n$  in Eq. (5) are expressed in the Fick form while the fluxes of the ions  $\Gamma_i$  and electrons  $\Gamma_e$  are expressed in the drift-diffusion form as the following:

$$\Gamma = \mu E n - \nabla(Dn) \quad (6)$$

where  $\mu$  is mobility of ions and electrons in electric field,  $E$  is the electric field,  $n$  is density of the different species,  $D$  is diffusivity coefficient. In case of electron transport and electron energy transport the electron mobility  $\mu_e$ , electron energy mobility  $\mu_{en}$ , electron energy density  $n_{en}$ , electron diffusivity  $D_e$  and electron energy diffusivity  $D_{en}$  are substituted in Eq. (6). In the most models of this work we considered unmagnetized plasma with a reduced electron mobility coefficient defined as a scalar  $\mu_{red}=\mu_e n_e$  [As<sup>2</sup>/kg·m<sup>3</sup>], but in the presence of the magnetic field the electron and ion mobilities become tensors [22,23]. The electron diffusivity, energy mobility and energy diffusivity are defined via Einstein's relation for a Maxwellian electron energy distribution function (EEDF):

$$D_e = \mu_e T_e, \mu_{en} = (5/3) \mu_e, D_{en} = \mu_{en} T_e \quad (7)$$

where  $T_e$  is the electron temperature defined as  $T_e = (2/3) < \varepsilon >$ , where the mean electron energy  $< \varepsilon > \geq n_{en}/n_e$ .

The DC electron mobility  $\mu_e$  was obtained by solving the Boltzmann kinetic equation in the two-term approximation in COMSOL Multiphysics using the Boltzmann equation interface [22,25]. Seven reactions, including electrons (e), ground-state argon atoms (Ar), excited argon atoms ( $Ar^*$ ) and single-charged argon ions ( $Ar^+$ ) were included in the model as presented in Table 1.

The transport equations were constrained by Neumann-type boundary conditions. At the anodes, the wall boundary condition was imposed, prescribing the normal fluxes to the boundary based on the

thermal movement of electrons and ions. The sticking coefficient for both the  $Ar^+$  ions and the  $Ar^*$  excited atoms was set to 1, which corresponds to a 100% recombination/de-excitation probability. The electron emission from the cathode was modeled by mimicking thermionic emission in which the electron influx is provided as an input parameter of the model. At the same time the coefficient of secondary electron emission was set to zero as negligible in comparison with thermionic electron influx.

The Poisson equation constrained by Dirichlet-type boundary conditions was used for calculation the plasma potential distribution across the discharge tube from which the electric field was calculated from Maxwell equation:

$$\nabla \cdot (\epsilon_0 \epsilon_r E) = \rho_V \quad (8)$$

$$E = -\nabla V \quad (9)$$

where  $V$  is electric potential,  $\rho_V$  is space charge density.

At the cathode, the electric potential was set to zero while at the corresponding anode, the electric potential was given by arc electric circuit equation

$$V = V_0 - R_B I_p - C_B R_B \frac{\partial}{\partial t} V \quad (10)$$

where  $V_0$  is the voltage at the output from the DC power supply,  $I_p$  is the plasma current obtained by integrating the current density over the anode, and  $R_B$  is resistance of the ballast resistor in the DC circuit. In addition, the electric circuit includes the bypass capacitor  $C_B$  which improves the convergence in the ignition phase and does not influence the results as we are only interested in the stationary state.

Two different axisymmetric geometries were considered for this modeling as illustrated in Fig. 9. The model shown in Fig. 9a includes the cathode and three anodes: two of them, the mid anode and the remote (main) anode are positioned within a metallic cylindrical

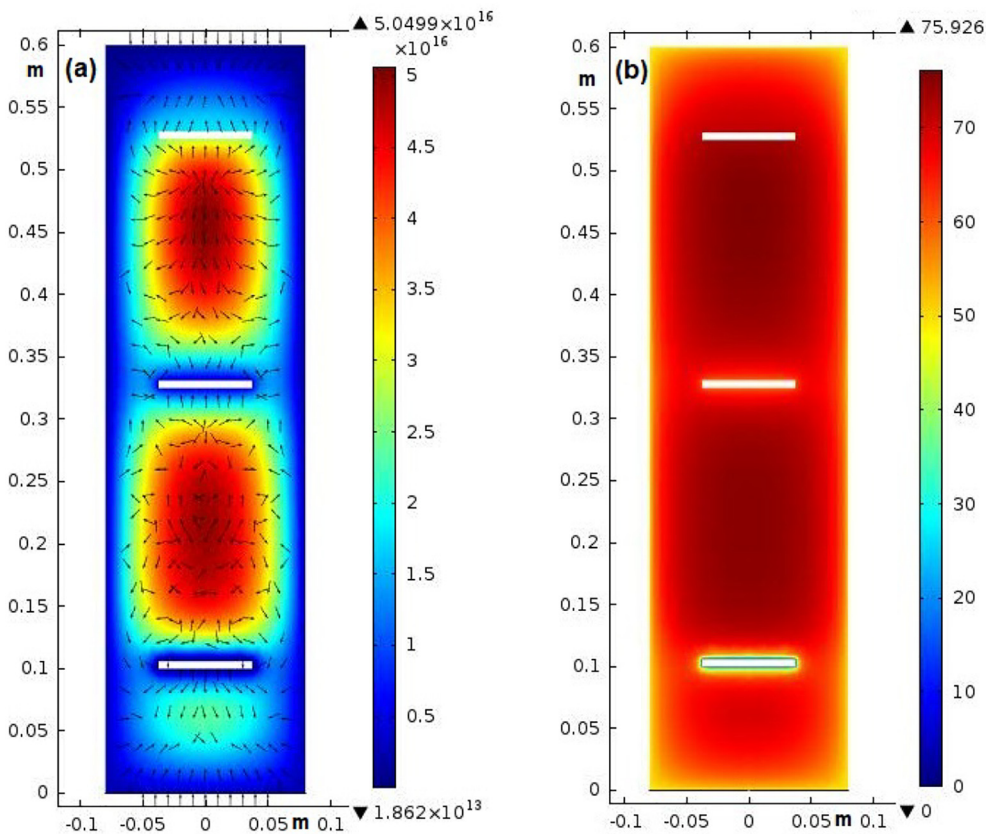


**Fig. 10.** Electron current density (shown by the arrows) and electron density  $n_e$  (a) and plasma potential  $V_p$  distribution (b) across the discharge tube with three anodes: RA, MA and WA.

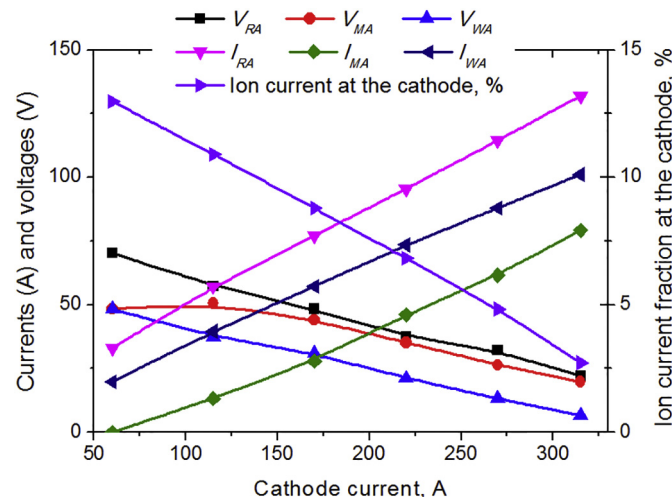


**Fig. 11.** Modeled anode currents and voltages as functions of the cathode current with  $4 \cdot 10^{-3}$  Torr in the cascaded arc discharge with three anodes: remote anode (RA), mid anode (MA) and wall anode (WA); also shown is the fraction of ion current at the cathode as a function of the cathode current.

discharge tube, 0.6 m long  $\times$  0.16 m diam. The metallic walls of the discharge tube served as the third, the primary anode, while both the cathode, mid anode and remote anode are made of thin disks, 0.075 m diam  $\times$   $6 \cdot 10^{-3}$  m thick and in some calculation as thin as  $2 \cdot 10^{-3}$  m.

The model with three anodes shown in Fig. 9a was solved for the thermionic current densities ranging from 0.5 to  $4 \text{ A/cm}^2$  uniformly distributed across the cathodes, which corresponds to the total thermionic currents ranging from 50 to 300 A, while the input voltages in

the remote anode, mid anode and wall anode circuits were taken at 90 V and 60 V respectively, mimicking the actual parameters of the experimental cascaded arc circuits. The ballast resistor was set to  $R_b = 0.5$  Ohm for all anodes, typical for the welder-style arc power supplies and the blocking capacitor was set to  $C_b = 1 \mu\text{F}$  for all anode circuits. The voltage current characteristics were calculated for all the anodes and the plasma parameters  $n_e$ ,  $T_e$  and  $V_p$ , were taken both across whole discharge tube and at two probe-points located on discharge axes, probe 1 between the cathode and the mid-anode and probe 2 between the mid-anode and the remote anode as illustrated in Fig. 9a. In the model presented in Fig. 9b with one single remote anode, the cathode is shielded by the floated chevron baffles.

The electron density  $n_e$ , the density of the electron current  $J_e$  and plasma potential  $V_p$ , shown in Fig. 10, are distributed quite evenly in the two regions - one between the cathode and the mid-anode and other between the mid-anode and the remote anode. This demonstrates the usage of a cascaded arc setup for extending the remote arc discharges along large discharge tubes, as also demonstrated experimentally [15].

The anode currents and voltages as well as the fraction of the ion current at the cathode are shown in Fig. 11 as functions of the cathode current at  $4 \cdot 10^{-3}$  Torr argon pressure. As it can be seen, all the anode currents increase while the ion fraction of the total cathode current decrease when the cathode current increases. Furthermore, the voltages of all anodes decrease with increase of the cathode current. All of the anode voltages (RA, MA and WA) decreased with increasing current to that anode as illustrated in Fig. 12. Thus, the high-current low-pressure cascaded arc discharge has a falling I-V characteristics both as a function of the total arc current generated by the cathode and also as a function of the local arc currents conducted to each of the chain of arc anodes. This was also seen in the drift-diffusion glow discharge models [26].

Falling I-V characteristics are typical for high pressure arc

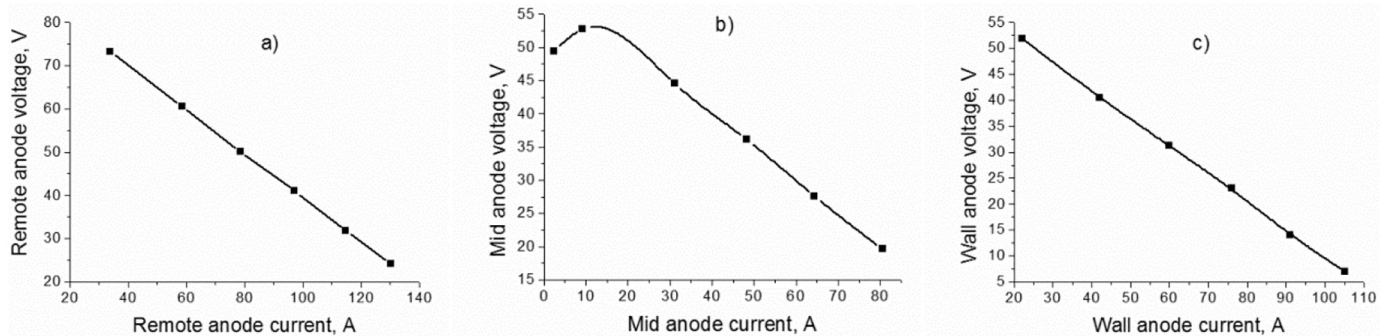


Fig. 12.  $I$ - $V$  characteristics of the RA (a), MA (b) and WA (c) versus their own currents in a cascaded arc discharge.

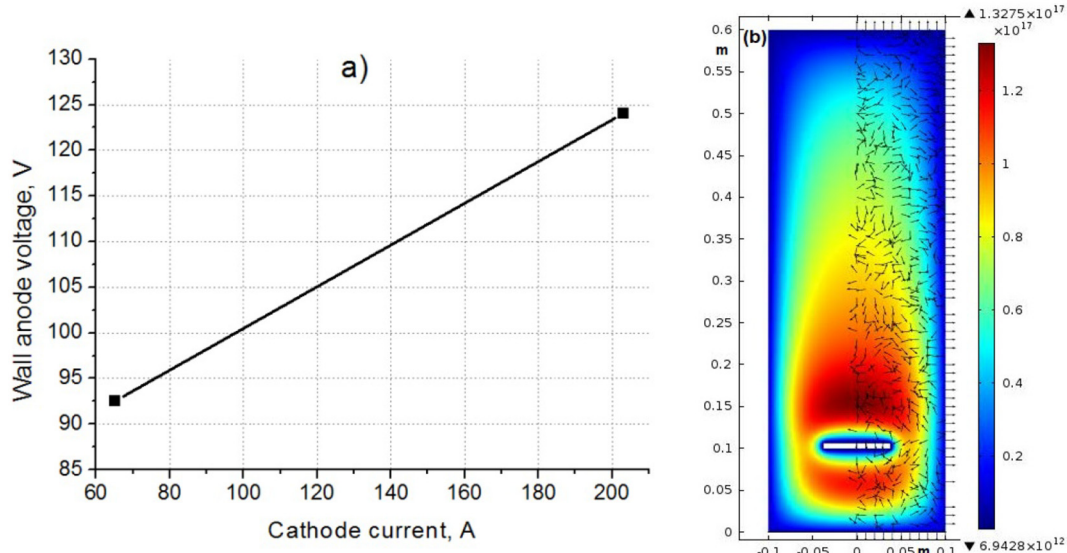


Fig. 13.  $I$ - $V$  characteristics (a) and distribution of electron density  $n_e$  and electron current density  $J_e$  shown by arrows on right side (b) in thermionic arc discharge in Ar at  $4 \cdot 10^{-3}$  Torr with one single wall anode (WA).

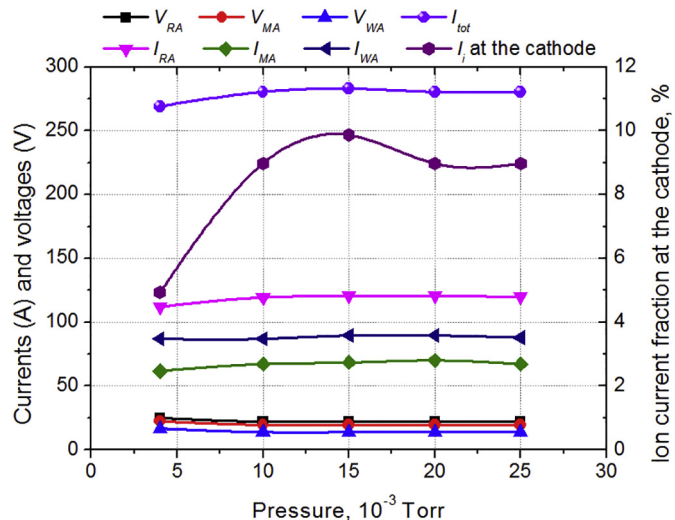


Fig. 14. Currents and voltages of RA, MA and WA, cathode current and the ion fraction of the cathode current as functions of pressure in a cascaded arc discharge with a thermionic current of 256 A.

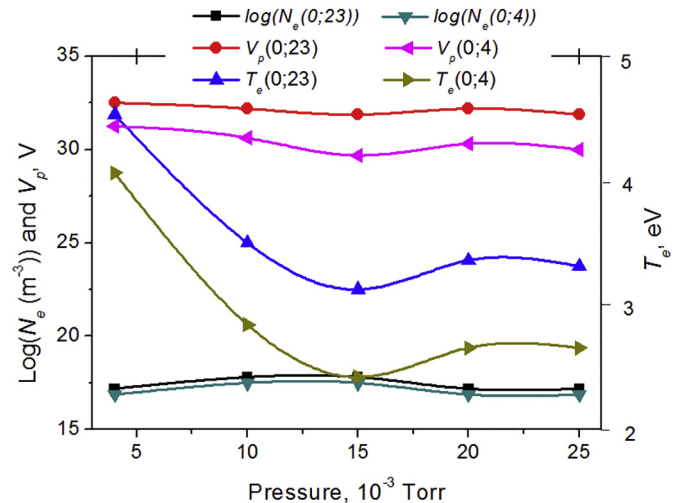


Fig. 15.  $n_e$ ,  $T_e$  and  $V_p$  in cascaded arc with RA, MA and WA as functions of pressure at two probe-points on discharge axes:  $z = 0.23$  m (1) between the cathode and MA and  $z = 0.4$  m (2) between MA and RA; argon pressure of  $4 \cdot 10^{-3}$  Torr, the thermionic current of 256 A.

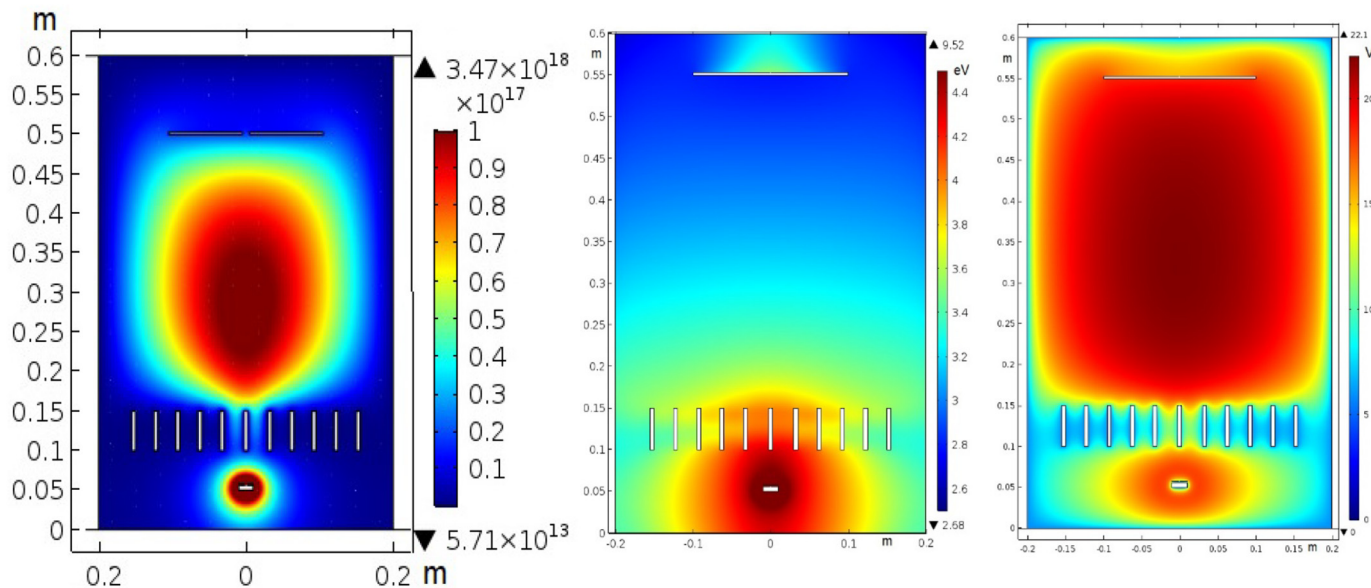


Fig. 16.  $n_e$ ,  $T_e$  and  $V_p$  with baffled primary anode electrically connected to the metal walls of the discharge tube and the remote anode.

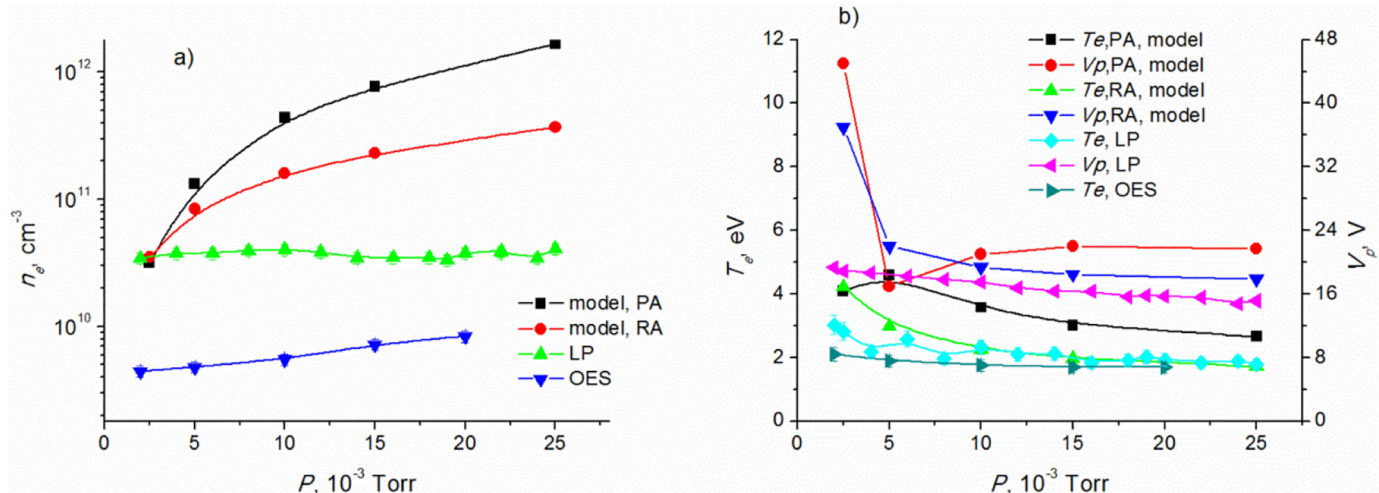


Fig. 17. Results of the modeling of the plasma parameters vs. experimental measurements in a remote arc discharge with a baffled miniature cathode and remote anode, as a function of pressure.

discharges driven by ohmic heating, thermal-conductivity, and radiation losses [15]. The difference between the falling  $I$ - $V$  characteristics obtained by the modeling and the rising  $I$ - $V$  of the remote arc discharge observed experimentally (Fig. 2a), where the discharge voltage increased slightly with increase of the arc current, can be attributed to neglecting the magnetic pinch effect in the high current remote arc plasma column in the model. Pinching of the arc discharge by the self-magnetic field creates a visible arc column, increases the current density and the arc column electrical resistance.

In contrast, the model  $I$ - $V$  characteristics of arc discharge between the cathode and the metal walls of the discharge tube without additional remote and mid-anodes shows the increase of the anode voltage when the arc current was increased, as shown in Fig. 13a.

The plasma density distribution across the arc discharge with a single wall anode shown in Fig. 13b demonstrates the rapid decrease of  $n_e$  along the axis of the discharge. This differs from the almost flat distribution of the electron density in the cascaded arc [15,26].

The anode currents and voltages and the cathode ion current fraction vs. pressure with a thermionic current influx of 256 A are shown in Fig. 14.

The remote anode and mid-anode currents increased slightly with pressure, while the potentials of the remote anode and mid-anode with respect to the cathode fell. This is typical for arc discharges and agrees well with the experimental finding. On the other hand, the currents and voltages of the primary anode are almost independent of pressure in the range  $(1\text{--}25) \cdot 10^{-3}$  Torr.

Shown in Fig. 15 are the plasma potential  $V_p$ , electron temperature  $T_e$  and  $n_e$  versus pressure at two probe-points along the discharge axis: between the cathode and the mid anode ( $z = 0.23$  m) and between the mid-anode and the remote anode ( $z = 0.4$  m) for a fixed thermionic emission current of 256 A (corresponding to the thermionic current density of  $2.5 \text{ A/cm}^2$ ).

The plasma density increased slightly when the pressure was increased. The plasma potential difference  $V_p$  across the discharge tube was close to the potentials of the RA and MA, considerably exceeding the wall anode potential WA, while the RA potential was slightly greater than that of the MA. The plasma potential decreased when the pressure was increased. The electron temperature  $T_e$  across the discharge tube did not exceed 5 eV, was highest near the cathode and decreased with increasing pressure. It demonstrates a small increase of

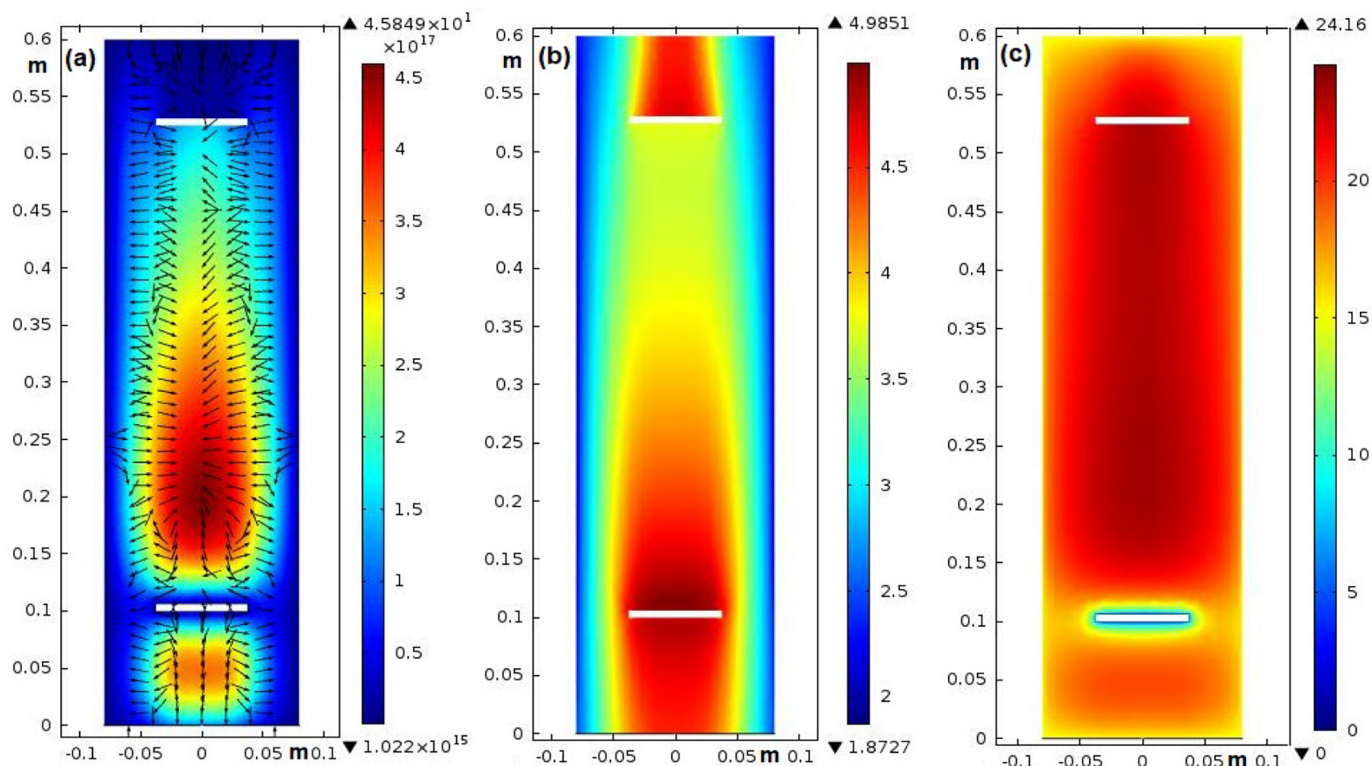


**Fig. 18.** Distribution of plasma parameters across a high-current low-pressure arc discharge under the influence of the self-magnetic field, at  $4 \cdot 10^{-3}$  Torr and 213 A cathode current: (a)  $n_e$ , (b)  $T_e$  and (c)  $V_p$ .

the plasma impedance with increase of the pressure. This behavior can explain the almost flat plasma density in the same pressure range  $(4\text{--}25) \cdot 10^{-3}$  Torr found by the Langmuir probe measurements and the small increase of the plasma density with increasing argon pressure found by OES.

The plasma density, electron temperature and plasma potential distribution across the modeled discharge tube with the baffled primary anode, consisting of a set of parallel thin rings all electrically connected to the metal walls, and the disk-shape remote anode as presented in the geometry illustrated in Fig. 9b are shown in Fig. 16.

The plasma density and the potential distribution is quite uniform across the area between the primary anode and remote anode, except for the thin plasma sheet areas attached to the surfaces of the electrodes, while the electron temperature is greater in the vicinity of the baffled primary anode and the cathode. This behavior was similar to that of the model with three anodes (geometry shown in Fig. 9a). It can be seen that the remote plasma cloud almost evenly filled the remote arc compartment (i.e. between the chevron baffle and the remote anode), while in the primary arc compartment (i.e. between the cathode and the chevron baffle) the plasma is dense only near the cathode.

Fig. 17 shows the model density and temperature of electrons as well as the plasma potential as functions of argon pressure in the low pressure DC arc discharge calculated near the primary and remote anodes and measured by the Langmuir probes positioned within the discharge tube in the corresponding locations near primary anode and near remote anode.

One can see that the temperature and density of electrons were higher near the primary anode than near the remote anode, with argon pressure  $\geq 3 \cdot 10^{-3}$  Torr. The electron temperature near the primary anode as well as near the remote anode decreased with pressure and, the electron density near both anodes increased with pressure. This phenomenon is well known: the increase in pressure increases ionization rate and a lower electron energy and temperature becomes

sufficient to maintain the discharge.

For the low-pressure high-current remote arc discharge, the dependence of the critical plasma parameters on pressure shown in Fig. 17, exhibits good qualitative and acceptable quantitative agreement with the experimental findings. As follows from these results, a decrease in the plasma temperature with increasing pressure is accompanied by an increase in the plasma density. At the same time, the plasma potential decreases indicating an increase of the electrical conductivity of the discharge plasma with an increase of the pressure. The comparison of model and experimental results shows weak sensitivity of the model to its given approximations, such as dimensions of the electrodes and its 2D axially-symmetrical geometry demonstrating the robust behavior of the model.

This modeling also shows that in the high-current low-pressure arc discharge, the arc current is conducted along the discharge axis, while the current density distribution is almost flat across the discharge tube. This allows the magnetic field within the arc column to be estimated. For the rough estimate of the influence of self-sustained magnetic field on arc column let us consider a case of a cathode current of 200 A evenly distributed across the discharge tube, the characteristic value of the magnetic field at the walls of the model tube of  $r = 0.08$  m is  $B = 5$  G, which can explain the formation of the arc column in long high-current low-pressure remote arc discharge by the self-induced pinch-effect, similar to the magnetically compressed arc plasma flows at higher pressures [27,28]. To estimate the possibility of the magnetic pinch-effect and formation of a well-defined arc plasma column under the influence of a self-induced magnetic field, a model with geometry similar to that shown in Fig. 9a, but without the mid anode, was solved at  $4 \cdot 10^{-3}$  Torr and a thermionic current density of  $2 \text{ A/cm}^2$ , while the magnetic field was calculated in assumption that the arc current is evenly distributed across the discharge tube. This gave the following expression for the axial longitudinal magnetic field across the discharge tube:  $B_z(r) = (\mu_0/2\pi)I_r/R^2$  where  $R$  is the radius of the discharge tube, while the radial component of the magnetic field  $B_r(r) = 0$ . In this

model the electron and ion mobilities were used in tensor form instead of the scalar mobilities of the non-magnetized plasma [22,23].

The results presented in Fig. 18 show the clear formation of a well-defined remote arc plasma column, which can explain the observation of the visible arc plasma constriction shown by the measurements of the dynamic ion current distribution in Fig. 3.

## 5. Conclusions

A study has been made of the low-pressure arc discharges in large chambers ignited between a planar vacuum arc cathode and both a surrounding grounded primary anode and a remote linear anode. The arc column moved up and down perpendicular to the cathode-anode direction, following the motion of the cathode spots. It was found that the cathode spot speed increased with the remote arc current and the corresponding increase of the total arc current, resulting in an increase of the arc steering magnetic field in agreement with the vacuum arc retrograde motion rule. The measurements of IEDFs with the retarding potential analyzer show that in the remote arc plasma there were two well-defined groups of ions, one consisting of ions having mean energy of several eV and another group with most probable ion energy  $\approx$  20 eV with FWHM  $\approx$  10–15 eV. The probe measurements showed great uniformity of the low-pressure arc parameters in the discharge cross sections.  $T_e$  and  $n_e$  measured with Langmuir probe were a bit higher than with the parameters obtained with OES methods. It was shown that  $T_e$  and  $n_e$  in the discharge rely more heavily on pressure and remote anode current and were less dependent on gas composition. N<sub>2</sub> dissociation degree in Ar-N<sub>2</sub> low-pressure arc discharges, as OES measurements shown, increases with Ar fraction in gas mixture. The most probable mechanism of N<sub>2</sub> dissociation in the low-pressure arc conditions is excitation transfer between Ar<sub>m</sub><sup>\*</sup> and N<sub>2</sub>. The analysis of the electron population in the remote arc discharge based on analysis of the second derivative of the Langmuir probe *I-V* characteristics allowed more accurate measurement of the electron population parameters in the discharge including electron drift velocity, plasma potential, electron density and energy. Moreover, the low-pressure arc in the large volume was modeled in the axially symmetric drift-diffusion approximation using commercial COMSOL FEM software. Comparison of the calculated and measured dependences of the remote arc plasma parameters on argon pressure showed good agreement between measured and calculated values of the plasma parameters. The experimental study and computer modeling have demonstrated that arc plasma can be extended into long large-area discharge chamber by using a set of remote anodes forming a cascaded arc discharge. The experimentally observed formation of the constricted arc column in the high-current low-pressure long remote arc discharge is explained by self-induced pinch effect created by self-inflicted magnetic field. More detailed modeling, taking into account the constriction of the high current arc plasma column by the magnetic pinch-effect created by the self-inflicted magnetic field will be a subject of future work.

## Acknowledgments

The authors are very grateful to Ray Boxman for detailed review and useful comments and suggestions, S. Pancheshnyi, V. M. Donnelly and Yi-Kang Pu for useful discussions, S. Myers, Z. Zembower and Jeff Opal, for their help with the experimental work and to Adam Obrusnik for his consultation on solver settings of the COMSOL plasma module.

## Funding

This research did not receive any specific grant from funding agencies in the public, commercial, or not-for-profit sectors.

## Appendix A. Supplementary data

Supplementary data to this article can be found online at <https://doi.org/10.1016/j.sab.2020.105785>.

## References

- [1] D. Degout, G. Farges, E. Bergmann, D. Dupont, High current density triode magnetron sputtering, *Surf. Coat. Technol.* 57 (1993) 105.
- [2] K. Otani, N. Sakata, T. Ozaki, K. Kawabata, Effects of magnetic flux density and substrate temperature on Ni films prepared by means of unbalanced magnetron sputtering assisted by inductively coupled plasma, *J. Phys. Conf. Ser.* 417 (2013) 012035.
- [3] S. Avtaeva, V. Gorokhovsky, S. Myers, S. Robertson, E. Shunko, Z. Zembower, Characterization of the large area plane-symmetric low-pressure DC glow discharge, *Spectrochim. Acta B* 124 (2016) 25.
- [4] V. Gorokhovsky, P. Del Bel Belluz, Ion treatment by low pressure arc plasma immersion surface engineering processes, *Surf. Coat. Technol.* 215 (2013) 431.
- [5] H. Böhrk, M. Auweter-Kurtz, Velocity and total pressure measurements in the two-stage hybrid thruster Tithus, *Prog. Propuls. Phys.* 1 (2009) 381.
- [6] M. Geva, M. Krishnan, J.L. Hirshfeld, Element and isotope separation in a vacuum-arc centrifuge, *J. Appl. Phys.* 56 (1984) 1398.
- [7] S.A. Barengolts, G.A. Mesyats, D.L. Shmelev, Mechanism of ion flow generation in vacuum arcs, *J. Exp. Theor. Phys.* 93 (2001) 1065.
- [8] A. Anders, The evolution of ion charge states in cathodic vacuum arc plasmas: a review, *Plasma Sources Sci. Technol.* 21 (2012) 035014.
- [9] B. Jüttner, Cathode spots of electric arcs, *J. Phys. D: Appl. Phys.* 34 (2001) R103.
- [10] R. Boxman, P. Martin, D. Sanders (Eds.), *Handbook on Vacuum Arc Science and Technology*, Noes Publications, NJ, 1995.
- [11] H. Pfister, W. Gekelman, Z. Lucky, J. Bamber, D. Leneman, J. Maggs, Design, construction, and properties of the large plasma research device-the LAPD at UCLA, *Rev. Sci. Instrum.* 62 (1991) 2875–2883.
- [12] D. Leneman, W. Gekelman, J. Maggs, The plasma source of the large Plasma device at University of California, Los Angeles, *Rev. Sci. Instrum.* 77 (2006) 015108.
- [13] L.M. Awasthi, G. Ravi, V.P. Anitha, P.K. Srivastava, S.K. Mattoo, A large area multifilamentary plasma source, *Plasma Sources Sci. Technol.* 12 (2003) 158–164.
- [14] Y.C. Hong, S.C. Lee, H.S. Uhm, Generation and diagnostics of large-volume plasmas, *J. Korean Phys. Soc.* 44 (2004) 1039–1043.
- [15] V. Gorokhovsky, S. Robertson, Low Pressure Cascaded Arc Discharge, Poster Presentation at the ICOPS45, Denver, (2018).
- [16] R.L. Stenzel, Microwave resonator probe for localized density measurements in weakly magnetized plasmas, *Rev. Sci. Instrum.* 47 (1976) 603.
- [18] I.H. Hutchinson, *Principles of Plasma Diagnostics*, 2nd ed., Cambridge University Press, New York, 2002.
- [19] X.M. Zhu, Y.K. Pu, Optical emission spectroscopy in low-temperature plasmas containing argon and nitrogen: determination of the electron temperature and density by the line-ratio method, *Top. Rev. J. Phys. D: Appl. Phys.* 43 (2010) 403001.
- [20] E.V. Shun'ko, *Langmuir Probe in Theory and Practice*, Universal Publishers, Boca Raton, FL, USA, 2009.
- [21] G.G. Raju, *Gaseous Electronics Theory and Practice*, CRC Press, Taylor & Francis, Boca Raton, FL, 2006.
- [22] COMSOL, *Plasma Module User's Guide*, (2012).
- [23] G.J.M. Hagelaar, N. Oudini, Plasma transport across magnetic field lines in low-temperature plasma sources, *Plasma Phys. Control. Fusion* 53 (2011) 124032.
- [24] A.V. Phelps, <ftp://jila.colorado.edu/collisionsdata/>.
- [25] G.J.M. Hagelaar, L.C. Pitchford, Solving the Boltzmann equation to obtain electron transport coefficients and rate coefficients for fluid models, *Plasma Sources Sci. Technol.* 14 (2005) 722–733.
- [26] V. Gorokhovsky, Modeling of DC Discharges in Argon at Low Pressures, Poster Presentation at the 12th Intern. COMSOL Conf., Boston, (2012).
- [27] W. Finkelburg, H. Maekker, *Electrische Bogen und Thermisches Plasma*, Handbuch der Physic, Bd. XXII, (1956), pp. 254–444.
- [28] H. Maecker, Plasmaströmungen in Lichtbögen infolge eigenmagnetischer Kompression, *Z. Phys.* 141 (1955) 198–216.